Disordered Cubic Spinel Structure in the Delithiated Li$_2$MnO$_3$ Revealed by Difference Pair Distribution Function Analysis

Masatsugu Oishi,[*, †] Keiji Shimoda,[‡] Koji Ohara,[*, §] Daiki Kabutan,[†] Tomoya Kawaguchi,[∥]

and Yoshiharu Uchimoto[⊥]

[†]*Graduate School of Technology, Industrial and Social Sciences, Tokushima University,* 2-1 *Minami Josanjima-cho, Tokushima, 770-8506, Japan*

[‡]*Office of Society-Academia Collaboration for Innovation, Kyoto University, Gokasho, Uji, Kyoto 611-0011, Japan*

[§]*Diffraction and Scattering Division, Japan Synchrotron Radiation Research Institute (JASRI), 1‑1‑1 Kouto, Sayo-cho, Sayo-gun, Hyogo 679‑5198*

[∥]*Institute for Materials Research, Tohoku University, 2-1-1, Katahira, Aobaku, Sendai 980-8577, Japan*

[⊥]*Graduate School of Human and Environment Studies, Kyoto University, Yoshida Nihonmatsu-cho, Sakyoku, Kyoto 606-8501, Japan*

[*]**Corresponding author**:
Masatsugu Oishi
Address: 2-1 Minami Josanjima-cho, Tokushima 770-8506, Japan
Phone: +81-88-656-7367
E-mail: ooishi.masatsugu@tokushima-u.ac.jp

ABSTRACT

An archetypical Li-rich layered oxide, Li_2MnO_3, shows a large initial charge capacity of ~350 mAh g^{-1} with little oxidation of the constituent Mn ions, yet, the crystal structure of delithiated Li_2MnO_3 is still unclarified because the structural disorder induced by the considerable Li extraction makes the analysis challenging. X-ray pair distribution function (PDF) analysis is a powerful tool to experimentally elucidate the structure of the disordered phase. Here, we conducted a comprehensive analysis with a focus on PDF analysis in combination with the X-ray powder diffraction (XRPD), transmission electron microscopy (TEM), and X-ray absorption spectroscopy (XAS) to reveal the disordered crystalline structure of the electrochemically delithiated Li_2MnO_3. The XRPD and TEM analyses clarified the formation of a low-crystallinity phase in the light of the average structure. The XAS and PDF analyses further revealed that the MnO_6–based framework was rearranged with maintaining the MnO_6 octahedral coordination after the initial charge. The difference pair distribution function (d-PDF) technique was therefore employed to extract the structural information of the low-crystallinity disordered phase. The delithiated phase was found to have a structure similar to the cubic spinel, $LiMn_2O_4$, rather than that of delithiated $LiMn_2O_4$ (λ-MnO_2). In addition, the middle-range order of the delithiated phase deteriorated after the charge, indicating a decrease of coherent domain size to a single nm order. The composite structure formed after the first charge, therefore, consists of the disordered cubic spinel structure and unreacted Li_2MnO_3. The formation of the composite structure "activates" the electrode material structurally and eventually induces characteristic large capacity of this material.

1. INTRODUCTION

Tremendous efforts have been devoted to studies concerning Li-rich layered oxides, the Li_2MnO_3–$LiMeO_2$ (*Me*=Ni, Co, and Mn) system, for nearly the past two decades, [1-5] and this materials system is still gathering attention as a promising candidate for a high capacity positive material for next-generation lithium-ion batteries (LIBs). The most studied Li-rich layered oxide is a composite Li_2MnO_3–$LiNi_{1/3}Co_{1/3}Mn_{1/3}O_2$ material. Compared to the capacities of 160 mAh g^{-1} for the conventional layered oxides such as $LiCoO_2$ and $LiNi_{1/3}Co_{1/3}Mn_{1/3}O_2$, the Li_2MnO_3–$LiNi_{1/3}Co_{1/3}Mn_{1/3}O_2$ material shows capacity as high as 250 mAh g^{-1}. Lu and Dahn[1] reported that the large capacity of the Li-rich layered manganese oxide is induced by an irreversible reaction that forms an oxygen-deficient material in the initial charging process. Namely, it shows a characteristic voltage profile in the 1st charging process: a voltage plateau where oxygen anions contribute to the charge compensation. In addition, crystal rearrangement is considered to take place by oxygen evolution and cation migration.[6-8] After the 1st irreversible process, a large amount of Li ions are reversibly extracted and inserted into the material, allowing it to show a higher capacity than conventional layered oxides.

We have reported the charge compensation mechanism of $Li_{1.16}Ni_{0.15}Co_{0.19}Mn_{0.50}O_2$ [9,10] and Li_2MnO_3[11] using hard and soft X-ray absorption spectroscopy (XAS). For the $Li_{1.16}Ni_{0.15}Co_{0.19}Mn_{0.50}O_2$ electrode, the soft XAS analysis revealed that the Ni, Co, and Mn cations stay unchanged in the voltage plateau and O anions participated in the charge compensation. In the following reversible cycles, O anions also continued to participate in parallel with redox reactions of Ni, Co, and Mn cations.[10] In Li_2MnO_3, we observed the reduction of Mn ions even though the delithiation continues in the 1st irreversible charging process. In the following reversible cycles, we confirmed the reversible participation of Mn cations and O anions, and the differential XAS analysis showed that O *K*-edge XAS peaks, whose energies were similar to peroxide, appeared in and then disappeared during the reversible

redox cycles. [11] Tarascon and co-workers[12-15] investigated the anion redox reaction in Li_2MeO_3, where the *Me* ions are 4d and 5d transition metal ions. Those large ions are heavily hybridized with O 2p orbitals, thereby preventing the evolution of oxygen ions from the crystal lattice during the oxidation process. They insisted that the oxidation of O^{2-} ions to form peroxo-like species and oxygen–oxygen (O–O) bonding occur in the layered oxides. These results indicated that the reorganization of the O network in the crystal structure occurs during the O anion redox reactions. Kubobuchi *et al*.[16] reported, from XAS and ab initio multiplet calculation results of Li_2MnO_3, that Mn^{4+} states are unchanged (not further oxidized) but the local structure around Mn^{4+} changes after the de-intercalation.

Since the first report on the composite material system of Li_2MnO_3–$LiCoO_2$ by Numata *et al*.[4] in 1999, there have been many research reports of Li_2MnO_3-based composite materials, and its specific electrochemical reaction mechanism is widely recognized. However, an accurate explanation concerning the crystal structure changes that occur during the redox reaction of O anions has not been shared among the researchers. This is mostly due to the low crystallinity or disordered states of the sample after the crystal rearrangements, i.e. structural activation, that occur during the 1st charging process, which prevents detailed structural characterization. Many papers have reported spinel-like phases formed by the extraction of Li ions from the composite materials.[17-26] In particular, the formation of spinel-like phases on the particle surface is often reported, but it is open to question since the electrochemical properties of Li_2MnO_3 and $LiMn_2O_4$ are different from each other. Therefore, we presume that the newly formed solid-solid hetero-interfaces of the composite materials play an important role in these electrodes, or the bulk properties of the newly formed phase are significantly different from those of the original phase. We have examined the atomic column images of Li_2MnO_3 using scanning transmission electron microscopy (STEM) techniques.[27] The electron energy loss spectroscopy (EELS) and high-angle annular dark field (HAADF) images indicated the two

structural domains of the pristine Li_2MnO_3 and Li-poor defect spinel phases in a single particle of a half-charged electrode. Therefore, we concluded that the electrochemical activation of Li_2MnO_3 involves the formation of the spinel-like phase, which is associated with the oxygen loss from the pristine structure and the spontaneous Mn migration into the vacant Li layer site that occur with the partial oxidation of the lattice O and the reduction of Mn valences. However, detailed structural information of the obtained Li-poor spinel structure was not obtained. This was because the obtained structure was highly disordered and its details could not be clarified by standard crystal structure analysis.[17] In addition, the TEM observation only probes the local structure of the observed sample, and hence, the average structural information is still not clarified. While pair distribution functional (PDF) analysis by total scattering directly provides structural information on the irregular atomic arrangements in amorphous materials as well as the ordered atomic arrangements in crystalline materials. Hence, PDF analysis is a powerful tool to experimentally elucidate the mixed structure composed of the ordered/disordered phases.

In this study, we elucidated the mixture of crystalline and amorphous states by the PDF analysis in Li_2MnO_3. The crystal structure changes proceeding during the charging and discharging process in Li_2MnO_3 were evaluated by applying difference PDF (d-PDF) analysis to bring to light a spinel-like phase obtained by the structural rearrangements. The details of this phase obtained from the structural refinement using the d-PDF profile are further discussed. In addition, the electronic structure and local structure were evaluated using X-ray absorption spectroscopy (XAS) and TEM to comprehensively elucidate the delithiated states of Li_2MnO_3.

2. EXPERIMENTAL SECTION

Li_2MnO_3 was prepared by the solid phase method from $LiOH \cdot H_2O$ (High Purity Chemicals, 99%) and $MnCO_3$ (High Purity Chemicals, 99.9%). The powder of each starting compound was carefully weighed at an appropriate ratio of Li: Mn = 2: 1, and calcined at 700 °C

for 24 hours. A conductive additive and a binder were added to the obtained powder to prepare a mixed positive electrode. A battery composed of a positive electrode, a negative electrode, a reference electrode (lithium foil), a separator, and an electrolytic solution (1 M $LiPF_6$, EC/EMC=3/7 vol.) was prepared. The charge-discharge evaluation was carried out at room temperature with a cut-off voltage of 2.0–4.8 V vs. Li^+/Li^0. The batteries after charging and discharging were disassembled in an Ar atmosphere glove box, and the electrodes were washed with DMC and dried under vacuum.

The X-ray powder diffraction (XRPD) experiments (Smart Lab; Rigaku) were performed using a Mo $K\alpha$ source at room temperature. The electrode powders were sealed in glass capillary tubes in an Ar-filled glove box for the measurements to avoid exposing the samples to an air atmosphere.

The select area electron diffraction (SAED) patterns were obtained with a field-emission transmission electron microscope (FE-TEM, HF-2200; Hitachi). The samples were sliced thin by a focused ion beam (FIB, nanoDUET NB5000; Hitachi High-Technologies) and placed on a copper mesh and then transferred into the microscope. All these treatments were performed under a vacuum or an Ar atmosphere.

The X-ray absorption spectroscopy (XAS) was performed in a transmission mode at the beamline BL28XU of the synchrotron radiation facility SPring-8 (Sayo, Japan). A Si (111) double crystal monochromator was used for Mn K-edge XAS measurements. The electrode samples were sealed in Al laminates in the glove box.

The high-energy X-ray total scattering experiments were carried out at the SPring-8 beamline BL04B2 using a two-axis diffractometer.[28, 29] The incident X-ray energy obtained via a Si (220) crystal monochromator was 61.4 keV. The electrode powders were sealed in the capillary tubes in the glove box under the Ar gas atmosphere. The measurements were performed in the transmission geometry with a 2θ angle from 0.3 to 49°, corresponding to a Q-

range from 0.2 to 25 Å^{-1}. The PDF profiles were obtained using the in-house BL04B2 software. The X-ray total structure factor, $S(Q)$, was derived from the scattering intensity. Then, the reduced PDF, $G(r)$, was obtained by the Fourier transformation of $S(Q)$:

$$G(r) = \frac{2}{\pi} \int_{Q_{\min}}^{Q_{\max}} Q\{S(Q) - 1\}\sin(Qr)dQ.$$

where $Q_{\max}$ and $Q_{\min}$ are the maximum and minimum Q value observed, respectively.

3. RESULTS

3.1 X-ray powder diffraction

Figure 1(a) shows the charge-discharge profiles of the Li_2MnO_3 electrode. A voltage plateau in the 1st charging process is the typical irreversible reaction observed in the Li-rich layered oxides. The subsequent cycles after the 1st discharge process indicated the reversible reactions. We also examined charge-discharge profiles of the spinel $LiMn_2O_4$ under the same cut off conditions (Fig.S1). The voltage profiles of Li_2MnO_3 and $LiMn_2O_4$ differed in the reversible cycles after the 1st charging process, although the phase transformation of Li_2MnO_3 to the spinel phase has been reported.[17-27]

Figure 2 shows XRPD profiles of the Li_2MnO_3 electrodes in the pristine state, and the charged and discharged states of the 1st, 2nd, and 5th cycles. All the peaks in the pristine state were ascribed by the layered structure with the monoclinic symmetry (space group: $C2/m$), in which Li and transition metal are alternatingly layered with separated by oxygen layers.[17] After the 1st charge at 4.8 V (1C_4.8 V), all the peaks became drastically weaker and broader, indicating disordering of the crystal structure. After the 1st discharge (1D_2.0 V), the peaks slightly sharpened and their intensity recovered in comparison with those of the 1st charge (1C_4.8 V) whereas they did not completely return to the original pristine state. The peaks in 9–15° observed in the pristine Li_2MnO_3 almost disappeared after the 1st charge and slightly recovered after the 1st discharge. These peaks are associated with the interlayer Li/Mn ordering

in the transition layers. Irreversible structural rearrangements, therefore, proceeded in the 1st cycle. After the subsequent cycles, the changes of the XRPD profile were nearly reversible between the charged and discharged states while further broadening of the peaks was observed in the 5th cycles, indicating the increase of the volume fraction of the disordered phases.

3.2 TEM observation

Figure 3 shows the SAED patterns from the micro-sized secondary particles of the pristine state, charged and discharged states of the 1st cycle (See also Figs.S2–4). The Debye rings of the pristine state were sharp, and its pattern was explained by the monoclinic *C2/m* structure (Fig.3(a))). After the 1st charge (1C_4.8 V), the Debye rings became blurred (Fig.3(b)) which corresponds to the present XRD observation discussed before. The monoclinic-like pattern was again observed in the subsequent 1st discharged state (1D_2.0 V), indicating the partial recovery of the Li_2MnO_3 structure (Fig.3(c)).

Figure 4 shows the bright field (BF)-STEM images and SAED patterns from hundreds-nm-sized particles of the pristine, 1st charged and 1st discharged states (See also Figs.S5 FFT patterns). The pristine state was the monoclinic structure (*C2/m*) with stacking faults judging from the SAED pattern and its streaks along the [001] direction. According to the TEM-EELS analysis, the peak position of the Mn *L*-edge was close to that of MnO_2, implying that Mn in the pristine state was the tetravalent state (Fig. S6). The diffraction spots became blurred and stretched in the 1st charged state shown in Fig.4(b) while no distinct amorphous phase was observed judging from the SAED pattern. The FFT patterns in the nano-sized range suggested different bond distances coexisting in the particle. The valence state of Mn was the trivalent state judging from the peak position of the Mn *L*-edge in the TEM-EELS analysis (Fig. S7). The SAED pattern of STEM at the 1st discharged state was characterized as the monoclinic structure (*C2/m*) (Fig.4(c)), consistent with the SAED pattern of the secondary particle

(Fig.3(c)). The diffraction spots were blurred in comparison with the pristine state, implying a distorted crystal structure. The corresponding TEM-EELS indicated that Mn was slightly reduced by discharging from a careful comparison of the spectrum of the 1st charged state (Fig. S8).

3.3 XAFS measurements

Figure 5 shows the Mn K-edge X-ray absorption near edge structure (XANES) spectra of the pristine Li_2MnO_3, and the 1st, 2nd, and 5th charged and discharged samples. The spectrum shape drastically changed after the 1st charge, implying that the local structure around Mn changed significantly during the first charging as the irreversible process. In addition, the electronic structure of the 1st charged state is different from the pristine state. However, since the spectra shape is different between the two states, it is difficult to discuss the valence changes only from these results. The charge compensation reaction in the 1st charge process is discussed more in detail with other results in DISCUSSION. On the other hand, the spectrum of the 1st discharged state was similar to that of the 1st charge state while its absorption edge shifted to lower energy. Thus, Mn was slightly reduced with maintaining the local structure in discharging. In the subsequent 2nd and 5th cycles, the Mn ions showed the reversible oxidation and reduction in the charging and discharging processes judging from the reversible absorption edge shifts.

3.4 PDF analysis

X-ray total structure factor profiles, $S(Q)$, of Li_2MnO_3 samples are shown in Fig. 6. All the peaks became weaker and broader after the 1st charge as observed in the conventional XRPD in Fig.2, suggesting the deterioration of crystallinity after the 1st charging process. Figure 7 shows $G(r)$ profiles of the pristine Li_2MnO_3, and the 1st charged and discharged samples. Note that the interactions of Mn and O were dominantly observed in PDF because of

the low scattering ability of Li. The amplitude decreased after the 1st charge process as a whole, which suggests structural disordering. The $G(r)$ profiles at short-range distances are shown in Fig.7 (b). The distance of the first neighboring Mn–O, which corresponds to the first peak at 1.9 Å, stayed unchanged with charge, while the distance of the secondary neighboring Mn–Mn at r = 2.8 Å increased with charge. In contrast, both distances of the farther Mn–O at 3.5 Å and Mn–Mn distance at 4.9 Å decreased and increased, respectively, after charge. Note that the interactions of O–O, $r \sim 2.6$ Å for example, were barely visible because of the low scattering ability. The increase of Mn–Mn distance suggests that the MnO_6–based framework was rearranged, while constant Mn–O at $r = 1.9$ Å indicates the local coordination environment around Mn is maintained after the 1st charge.

After the 1st discharge, the amplitude did not completely recover to that of the pristine state, indicating the irreversible structural transformation in the 1st cycle. The distance of the first neighboring Mn–O stayed unchanged, while these of the farther correlations became long with the structural transformation after the 1st cycle. These results indicate that the disordering of the MnO_6–based framework, induced by the first charge, is irreversible. The peak positions were mostly unchanged between the 1st charge and discharge. On the other hand, after the 20th cycles, the correlation peaks at $r > 4$ Å shifted to longer distances with discharge (Fig. 8), suggesting the reduction of Mn that accompanies the increase of the ionic radius. The $G(r)$ profiles after 20 cycles were similar to that of the 1st cycle in the distances of the nearest- and second-nearest neighbors. However, the farther correlations changed after the cycles, which indicates the successive charge/discharge cycles yield irreversible structural disordering in the crystal host structure. (Fig. S9 (a) and (b)).

4. DISCUSSION

Our XRPD and SAED results showed that the layered structure of Li_2MnO_3 was highly

disordered after the 1st charge. The decreased diffraction intensity of the 1st charged state implies the formation of an amorphous or low-crystallinity phase. Hence, the ordered and disordered phases coexist in the charged material and form a composite microstructure after the structural activation in the 1st charging process. The ordered phase is attributed to the remaining Li_2MnO_3, and the disordered phase results from the delithiated phase. In the subsequent discharge, the crystalline order slightly recovered in comparison with the charged states. Namely, the reinsertion of Li would partially recover the crystalline order but the structure does not completely return to the pristine state. In the 2nd cycle, the XRPD peak intensities of the discharged state were stronger compared to the charged state, which also implies the recovery of the ordered phase of Li_2MnO_3 by the Li reinsertion. Such recovery of the ordered phase was not clearly observed in the 5th cycle, because the XRPD intensities were virtually similar between the charged and discharged states. This loss of the structural reversibility with cycles would be related to the cyclability deterioration of the over the cycles.

We further extracted the component of the delithiated phase from the PDF profiles in the charge material by the d-PDF method.[30] The Li_2MnO_3 electrode prepared for the high-energy X-ray total scattering measurements showed 381 mAh g^{-1} in the 1st charged state at 4.8 V, while its theoretical capacity is 459 mAh g^{-1}. Therefore, the difference between the theoretical capacity and the actual charge capacity is 78 mAh g^{-1}, which is 17% of the theoretical capacity. This corresponds to the unreacted Li_2MnO_3 phase in the 1st charged state by assuming that the contribution from undesirable side reactions is negligible and the charging dominantly proceeds as the two-phase reaction. Then, the reduced PDF profile at the 1st charged state at 4.8 V, $G_c(r)$, is given as

$$G_c(r) = 0.83 G_d(r) + 0.17 G_p(r)$$

(1)

where $G_d(r)$ and $G_p(r)$ are reduced PDF profiles of the delithiated and pristine Li_2MnO_3 phases,

respectively. Since $G_p(r)$ is known from the pristine state, the reacted component, $G_d(r)$, can be calculated from the present $G_c(r)$ (schematically shown in Fig.9). The $G_d(r)$ profile is compared with the PDF profile of the pristine $LiMn_2O_4$ ($Fd\bar{3}m$) cubic spinel structure in Fig. 10. The peak positions of the delithiated phase were in excellent agreement with those of $LiMn_2O_4$, while their amplitude was lower compared to that of $LiMn_2O_4$. The interatomic distances of the delithiated phase of charged Li_2MnO_3 are, therefore, similar to those of the $LiMn_2O_4$ cubic spinel structure. Note that the $G(r)$ profiles of the pristine Li_2MnO_3 are distinctively different from that of $LiMn_2O_4$ in the medium range ($r > 4$ Å) while they are apparently similar in the short-range structure ($r < 4$ Å) (Fig.S10). Also note that the d-PDF profile of the delithiated phase was different from that of the delithiated $LiMn_2O_4$ (i.e., λ-MnO_2) and pristine Li_2MnO_3 (Fig. S11). In addition, the intensity of $G(r)$ peaks of the delithiated phase gradually decayed with distance, which indicates the disorder in the long-range region that is potentially associated with both the decrease of crystalline size and the formation of amorphous domain. However, no distinct amorphous domain was observed in the BF-STEM images and diffraction patterns. In addition, the intensity of $G(r)$ peaks of the delithiated phase significantly decreased at $r > 20$ Å, implying a coherent length of the delithiated domain is as small as $r < \sim 2$ nm. Hence, the d-PDF result indicates that the delithiated domain is a nanoscale crystalline domain of disordered $LiMn_2O_4$ structure.

The lattice parameters of $LiMn_2O_4$ normally decrease by the Li extraction as previously reported from XRPD [31, 32] because of the smaller ionic radius of oxidized Mn ions in the delithiated material. Such decrease of the lattice parameter was also observed in the PDF study of $LiMn_2O_4$, in which all the peaks shifted toward shorter distance with charge (Fig. S12). The correlation distance in the delithiated domain of Li_2MnO_3 was similar to the stoichiometric $LiMn_2O_4$ despite the Li-defects. Also, the Mn valence state in the delithiated domain of Li_2MnO_3 was similar to that of the stoichiometric $LiMn_2O_4$ (+3.5) rather than that of Li-

deficient $LiMn_2O_4$ (~+4) as seen in the XANES study. Moreover, the reduction of Mn from +4 in the pristine Li_2MnO_3 to +3 with delithiation is counterintuitive, indicating that Mn does not compensate the electric charge during delithiation. Therefore, the other element in the material, O anion instead of Mn, should compensate the charge for the delithiation by changing its valance state and oxygen evolution reaction[11, 27]. Hence, the delithiated domain may possess some oxygen vacancies.

The Fourier transforms of the Mn K-edge EXAFS showed that the first and second peaks at ~1.5 and ~2.4 Å reflecting the Mn–O, and the mixture of the Mn–Mn and Mn–Li correlations, respectively, decreased after the 1st charge process, which suggested the structural disordering (Fig. S13(b)). This is consistent with results obtained in the $G(r)$ profiles already discussed and showed in Fig.7(b). The EXAFS was further fit by the structural model proposed by the d-PDF analysis, in which the charged material consists of the pristine Li_2MnO_3 and spinel $LiMn_2O_4$ structures. The EXAFS spectrum was successfully fit by the tow-phase model within the reasonable residual factor of 3.84%, which also demonstrates that the delithiated phase has a spinel structure with distorted Mn–Mn symmetry and the oxygen defects (Table. S3).

Our results showed that the Li_2MnO_3 is electrochemically activated by the crystal rearrangements accompanying the Li extraction, Mn migration, and some O_2 release, and eventually forms the composite microstructure of the ordered Li_2MnO_3 and disordered spinel-like phases. The cubic spinel-like structure of the delithiated Li_2MnO_3 is similar but not exactly the same as the $LiMn_2O_4$ cubic spinel structure judging from the electrochemical behavior of these materials (Fig.S1). During the activation process, the oxygen release and the oxidation of the lattice oxygen would also be a source of formation of disordered delithiated phase.[33-36] Furthermore, the $G(r)$ profile of the delithiated phase in the 1st cycle was in good agreement with that after the 20th cycle (Fig. S14) in terms of the peak positions and oscillation amplitude. This indicates that the ordered Li_2MnO_3 domain had been disappearing during the 20 cycles of

charge and discharge. The capacity degradation of Li_2MnO_3 after cycles is, therefore, attributed to the continuous and irreversible phase transformation from the ordered Li_2MnO_3 to the disordered $LiMn_2O_4$-like phase. The $G(r)$ peak intensities of the delithiated phase and 20th charged state were compared with those of the crystalline $LiMn_2O_4$ cubic spinel structure by the following equation:

$$\Delta G(r)\_peak = Gc(r)\_peak / G_{spinel}(r)\_peak \qquad (2)$$

where $Gc(r)\_peak$ is the $G(r)$ peak intensity of the delithiated phase and 20th charged state, and $G_{spinel}(r)$ peak is that of $LiMn_2O_4$. The $\Delta G(r)\_peak$ values are close to 1 where the correlation distance is short, and rapidly approaches 0 as the correlation distance increases (Fig.11). It implies that the medium-range correlation is smaller than that of the crystalline $LiMn_2O_4$. The small correlations are recognized at $r > 25$ Å for the delithiated phase, while they are observed at $r > 18$ Å at the 20th cycle. It indicates that the size of the ordered domain decreased with the cycles. The $\Delta G(r)\_peak$ values are smaller for the 20th sample compared to the 1st cycle implying the larger distortion after the 20 cycles, which corresponds to the irreversible structural disordering with the cycles. Note that these structural rearrangements observed in this study are phenomena in the bulk rather than a surface reaction because PDF analyses and XAFS technique reflects the bulk information of the sample.

The charged Li_2MnO_3 should be the Li poor state under the high oxidation states. Nevertheless, the interatomic correlations of the disordered phase in the charge Li_2MnO_3 were similar to the pristine $LiMn_2O_4$ cubic spinel structure. The Mn K-edge XANES spectrum in the 1st charged state indicates the little contribution of Mn to the charge compensation. Hence, the redox reaction of the O anion would balance the charge in the material during the Li extraction, which we reported previously from soft XAS study.[11] Since Mn rather than O generally compensates the charge during charge/discharge in $LiMn_2O_4$, the difference in the charge compensation mechanism of Li_2MnO_3 is related to the coexistence of the unique disordered

domain of the cubic spinel-like structure and the unreacted Li_2MnO_3 domain. Thus, a key to designing a large capacity positive material is to maintain this composite matrix in the subsequent cycles. We also showed that the d-PDF analysis is a practical and useable tool for elucidating the composite material composed of ordered and disordered phases.

5. CONCLUSION

We examined the structural variations of Li_2MnO_3 during the irreversible 1st cycle and the following reversible cycles. The XRPD and SAED measurements suggested the structural disordering of Li_2MnO_3 and the formation of a low-crystallinity phase in the 1st charge state. The structural information of the latter phase was successfully extracted from the d-PDF profile. The newly formed phase in the delithiated Li_2MnO_3 has a local structure similar to that of cubic spinel $LiMn_2O_4$, and different from that of the Li-poor $LiMn_2O_4$ (λ-MnO_2). In addition, the intensity of $G(r)$ peaks of the delithiated Li_2MnO_3 gradually decayed with distance, which determined the coherent length (domain size) of the disordered spinel phase. Hence, the disordered cubic spinel structure is formed after the initial structural activation of Li_2MnO_3 that contributes to the reversible extraction and insertion of the Li-ions. Therefore, a key to designing a large capacity positive material is to maintain the composite matrix in the subsequent cycles.

AUTHORS INFORMATION

Corresponding Authors

Masatsugu Oishi – *Graduate School of Technology, Industrial and Social Sciences, Tokushima University, 2-1 Minami Josanjima-cho, Tokushima, 770-8506, Japan;* ORCID: 0000-0002-4561-1038, E-mail: ooishi.masatsugu@tokushima-u.ac.jp

Koji Ohara – *Diffraction and Scattering Division, Japan Synchrotron Radiation Research*

Institute (JASRI), 1‑1‑1 Kouto, Sayo-cho, Sayo-gun, Hyogo 679‑5198; ORCID: 0000-0002-3134-512X, E-mail: ohara@spring8.or.jp

Authors

Keiji Shimoda – *Office of Society-Academia Collaboration for Innovation, Kyoto University, Gokasho, Uji, Kyoto 611-0011, Japan;* ORCID: 0000-0003-4600-3437

Daiki Kabutan – *Graduate School of Technology, Industrial and Social Sciences, Tokushima University, 2-1 Minami Josanjima-cho, Tokushima, 770-8506, Japan*

Tomoya Kawaguchi – *Institute for Materials Research, Tohoku University, 2-1-1, Katahira, Aobaku, Sendai 980-8577, Japan;* ORCID: 0000-0002-7600-4847

Yoshiharu Uchimoto – *Graduate School of Human and Environment Studies, Kyoto University, Yoshida Nihonmatsu-cho, Sakyoku, Kyoto 606-8501, Japan;* ORCID: 0000-0002-1491-2647

Author Contributions

M. O. and K. O. initiated the concept. M. O., K. O., and D. K. conducted the high-energy X-ray total scattering experiments and analyzed the data. M. O. and T. K. conducted the XAS experiments, and analyzed the data. M. O., K. S., and D. K. conducted the sample synthesis and the electrochemical experiments. Y. U. supervised the research. M. O., K. S., K. O. and T. K. wrote the manuscript. All authors have given approval to the final version of the manuscript.

Notes

There are no conflicts to declare.

ACKNOWLEDGEMENTS

REFERENCES

(1) Lu, Z; Dahn J. R., Understanding the Anomalous Capacity of Li/Li[Ni$_x$Li$_{(1/3-2x/3)}$ Mn$_{(2/3-x/3)}$]O$_2$ Cells Using In Situ X-Ray Diffraction and Electrochemical Studies, *J. Electrochem. Soc.* **2002**, 149, A815-A822.

(2) Thackeray M. M.; Kang S. H.; Johnson C. S.; Vaughey J. T.; Benedek R.; Hackney S. A. Li$_2$MnO$_3$-stabilized LiMO$_2$ (M = Mn, Ni, Co) electrodes for lithium-ion batteries, *J. Mater. Chem.* **2007**, 17, 3112-3125.

(3) Goodenough J. B.; Kim Y. Challenges for Rechargeable Li Batteries, *Chem. Mater.* **2010**, 22, 587-603.

(4) Numata N.; Sakakai C.; Yamanaka S. Synthesis and characterization of layer structured solid solutions in the system of LiCoO$_2$–Li$_2$MnO$_3$, *Solid State Ionics* **1999**, 117, 257–263.

(5) Ohzuku T.; Nagayama M.; Tsuji K.; Ariyoshi K. High-capacity lithium insertion materials of lithium nickel manganese oxides for advanced lithium-ion batteries: toward rechargeable capacity more than 300 mA h g^{-1}, *J. Mater. Chem.* **2011**, 21, 10179–10188.

(6) Armstrong A. R.; Holzapfel M.; Novak P.; Johnson C. S.; Kang S. H.; Thackeray M. M.; Bruce P. G. Demonstrating Oxygen Loss and Associated Structural Reorganization in the Lithium Battery Cathode Li[Ni$_{0.2}$Li$_{0.2}$Mn$_{0.6}$]O$_2$, *J. Am. Chem. Soc.* **2006**, 128, 8694-8698.

(7) Hy S.; Felix F.; Rick J.; Su W. N.; Hwang B. J. Direct In situ Observation of Li$_2$O Evolution on Li-Rich High-Capacity Cathode Material, Li[Ni$_x$Li$_{(1–2x)/3}$Mn$_{(2–x)/3}$]O$_2$ (0 ≤ x ≤0.5), *J. Am. Chem. Soc.* **2014**, 136, 999-1007.

(8) Tran N.; Croguennec L.; M. Ménétrier M.; Weill F.; Biensan Ph.; Jordy C.; Delmas C. Mechanisms Associated with the "Plateau" Observed at High Voltage for the Overlithiated Li$_{1.12}$(Ni$_{0.425}$Mn$_{0.425}$Co$_{0.15}$)$_{0.88}$O$_2$ System, *Chem. Mater.* **2008**, 20, 4815-4825.

(9) Oishi M.; Takanashi Y.; Fujimoto T.; Ina T.; Kawamura A.; Yamashige H.; Takamatsu D.; Orikasa Y.; Murayama H.; Tanida H.; Arai H.; Mineshige A.; Ishii H.; Ohta T.; Uchimoto

Y.; Ogumi Z. Charge compensation mechanisms in Li1.16Ni0.15Co0.19Mn0.50O2 positive electrode material for Li-ion batteries analyzed by a combination of hard and soft X-ray absorption near edge structure, *J. Power Source*s **2013**, 222, 45-51.

(10) Oishi M.; Yogi C.; Watanabe I.; Ohta T.; Orikasa Y.; Uchimoto Y.; Ogumi Z. Direct observation of reversible charge compensation by oxygen ion in Li-rich manganese layered oxide positive electrode material, Li1.16Ni0.15Co0.19Mn0.50O2, *J. Power Sources* **2015**, 276, 89-94.

(11) Oishi M.; Yamanaka K.; Watanabe I.; Shimoda K.; Matsunaga T.; Arai H.; Ukyo Y.; Uchimoto Y.; Ogumi Z.; Ohta T. Direct observation of reversible oxygen anion redox reaction in Li-rich manganese oxide, Li_2MnO_3, studied by soft X-ray absorption spectroscopy *J. Mater. Chem. A* **2016**, 4, 9293-9302.

(12) McCalla E.; Abakumov A. M.; Saubanère M.; Foix D.; Berg E. J.; Rousse G.; Doublet M.-L.; Gonbeau D.; Novák P.; Tendeloo G. V.; Dominko R.; Tarascon J.-M. Visualization of O-O peroxo-like dimers in high-capacity layered oxides for Li-ion batteries, *Science* **2015**, 350, 1516-1521.

(13) Rozier P.; Tarascon J. –M. Review—Li-Rich Layered Oxide Cathodes for Next-Generation Li-Ion Batteries: Chances and Challenges, *J. Electrochem. Soc.* **2015**, 162, A2490-A2499.

(14) Sathiya M.; Ramesha K.; Rousse G.; Foix D.; Gonbeau D.; Prakash A. S.; Doublet M. L.; Hemalatha K.; Tarascon J.-M. *Chem. Mater.* **2013**, 25, 1121–1131.

(15) Sathiya M.; Rousse G.; Ramesha K.; Laisa C. P.; Vezin H.; Sougrati M. T.; Doublet M.-L.; Foix D.; Gonbeau D.; Walker W.; Prakash A. S.; Ben Hassine M.; Dupont L.; Tarascon J.-M. Reversible anionic redox chemistry in high-capacity layered-oxide electrodes, *Nat. Mater.* **2013**, 12, 827–835.

(16) Kubobuchi K.; Mogi M.; Ikeno H.; Tanaka I.; Imai H.; Mizoguchi T. Mn $L_{2,3}$-edge X-ray

absorption spectroscopic studies on charge-discharge mechanism of Li_2MnO_3, *Appl. Phys. Lett*. **2014**, 104, 053906 (1-4).

(17) Yu Denis Y. W.; Yanagida K.; Kato Y.; Nakamura H. Electrochemical Activities in Li_2MnO_3, *J. Electrochem. Soc*. **2009**, 156 (6), A417-A424.

(18) Robertson A. D.; Bruce P. G. Mechanism of Electrochemical Activity in Li_2MnO_3,*Chem. Mater*. **2003**, 15, 1984-1992.

(19) Park S.-H.; Sato Y.; Kim J.-K.; Lee Y.-S. Powder property and electrochemical characterization of Li_2MnO_3 material, *Mater. Chem. Phys*. **2007***, 102, 225-230.

(20) Park S.-H.; Ahn H. S.; Park G. J.; Kim J.; Lee Y.-S. Cycle mechanism and electrochemical properties of lithium manganese oxide prepared using different Mn sources *Mater. Chem. Phys*. **2008**, 112, 696-701.

(21) Amalraj S. F.; Markovsky B.; Sharon D.; Talianker M.; Zinigrad E.; Persky R.; Haik O.; Grinblat J.; Lampert J.; Schulz-Dobrick M.; Garsuch A.; Burlaka L.; Aurbach D. Study of the electrochemical behavior of the "inactive" Li_2MnO_3, *Electrochim. Acta*, **2012**, 78, 32–39.

(22) Amalraj S. F.; Burlaka L.; Julien C. M.; Mauger A.; Kovacheva D.; Talianker M.; Markovsky B.; Aurbach D. Phase Transitions in Li_2MnO_3 Electrodes at Various States of-Charge, *Electrochim. Acta,* **2014**, 123, 395–404.

(23) Wang R.; He X.; He L.; Wang F.; Xiao R.; Gu L.; Li H.; Chen L.; Atomic Structure of Li_2MnO_3 after Partial Delithiation and Relithiation, *Adv. Energy Mater*. **2013**, 3, 1358–1367.

(24) Yan P.; Xiao L.; Zheng J.; Zhou Y.; He Y.; Zu X.; Mao S. X.; Xiao J.; Gao F.; Zhang J.-G.; Wang C.-M. Probing the Degradation Mechanism of Li_2MnO_3 Cathode for Li-Ion Batteries, *Chem. Mater*. **2015**, 27, 975–982.

(25) Phillips P. J.; Bareño J.; Li Y.; Abraham D. P.; Klie R. F. On the Localized Nature of the

Structural Transformations of Li_2MnO_3 Following Electrochemical Cycling, *Adv. Energy Mater.* **2015**, 5, 1501252(1-12).

(26) Koga H.; Croguennec L.; Mannessiez P; Ménétrier M.; Weill F.; Bourgeois L.; Duttine M.; Suard E.; Delmas C. $Li_{1.20}Mn_{0.54}Co_{0.13}Ni_{0.13}O_2$ with Different Particle Sizes as Attractive Positive Electrode Materials for Lithium-Ion Batteries: Insights into Their Structure, *J. Phys. Chem. C* **2012**, 116, 13497−13506.

(27) Shimoda K.; Oishi M.; Matsunaga T.; Murakami M.; Yamanaka K.; Arai H.; Ukyo Y.; Uchimoto Y.; Ohta T; Matsubara E.; Ogumi Z. *J. Mater. Chem. A* **2017**, 5, 6695-6707.

(28) Ohara S.; Onodera Y.; Kohara S.; Koyama C.; Masuno A.; Mizuno A.; Okada J. T.; Tahara S.; Watanabe Y.; Oda H.; Nakata Y.; Tamaru H.; Ishikawa T.; Sakata O. Accurate synchrotron hard X-ray diffraction measurement on high-temperature liquid oxides, *Int. J. Microgravity Sci. Appl.,* **2020**, 37(2), 370202.

(29) Kohara S.; Ohara K.; Temleitner L.; Ohishi Y. Fujiwara A.; Takata M. Structure of Disordered Materials Studied by High-Energy X-Ray Diffraction Technique, *Materials Science Forum* **2012**, 706-709, 1690-1695.

(30) Shiotani S.; Ohara K.; Tsukasaki H.; Mori S.; Kanno R. Pair distribution function analysis of sulfide glassy electrolytes for all-solid-state batteries: Understanding the improvement of ionic conductivity under annealing condition. *Sci Rep.* **2017**, 7, 6972.

(31) Ohzuku T.; Kitagawa M.; Hirai T. Electrochemistry of Manganese Dioxide in Lithium Nonaqueous Cell III . X - Ray Diffractional Study on the Reduction of Spinel - Related Manganese Dioxide *J. Electrochem. Soc.* **1990**, 137, 769-775.

(32) Thackeray M. M. Manganese oxides for lithium batteries*, Prog. Solids. Chem.* **1997**, 25, l-71.

(33) Sugiyama J.; Atsumi T.; Hioki T.; Noda S.; Kamegashira N. Nonstoichiometry and Defect Structure of Spinel $LiMn_2O_{4-\delta}$, *J. Power Sources* **1997**, 68, 641-645.

(34) Sugiyama J.; Atsumi T.; Hioki T.; Noda S.; Kamegashira N. Oxygen Nonstoichiomety of Spinel $LiMn_2O_{4-\delta}$, *J. Alloy Comp.*. **1996**, 235, 163-169.

(35) Yamada A.; Miura K.; Hinokuma K.; Tanaka M. Synthesis and Structure Aspects of $LiMn_2O_{4-\delta}$, as a Cathode for Rechargeable Lithium Batteries, *J. Electrochem. Soc.,* 1995, 142, 2149-2156.

(36) Suzuki K.; Barbiellini B.; Orikasa Y.; Go N.; Sakurai H.; Kaprzyk S.; Itou M.; Yamamoto K.; Uchimoto Y.; Wang Y. J.; Hafiz H.; Bansil A.; Sakurai Y. Extracting the Redox Orbitals in Li Battery Materials with High-Resolution X-Ray Compton Scattering Spectroscopy, *Phys. Rev. Lett.* **2015**, 114, 087401 (1-6).

Figures:
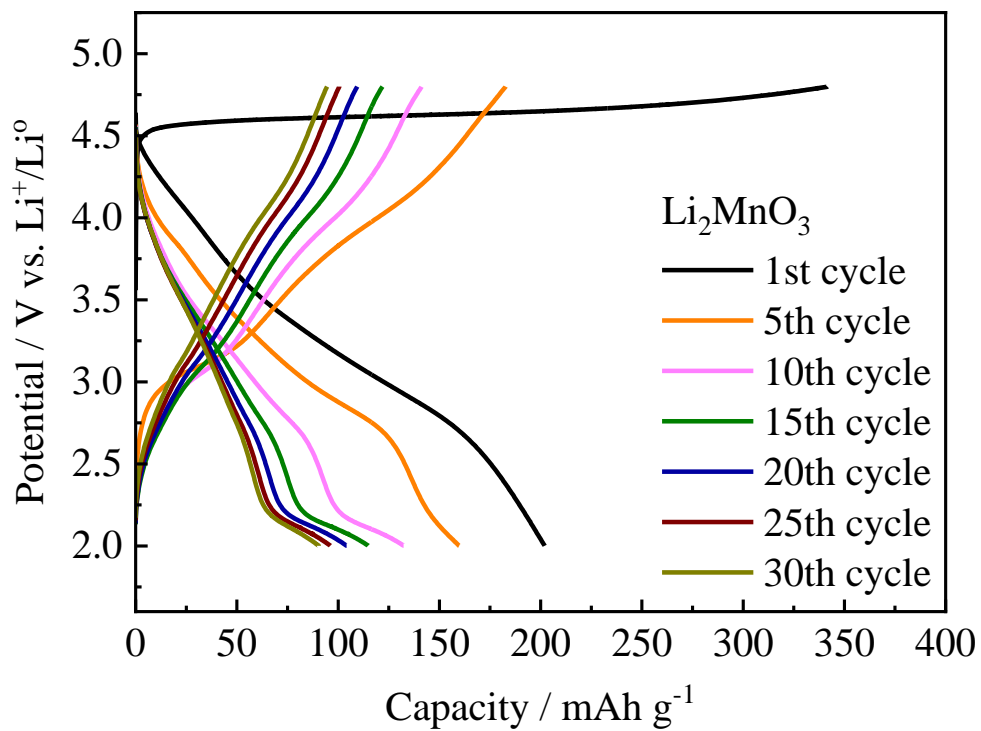
Figure 1. Charge–discharge profiles of Li_2MnO_3.
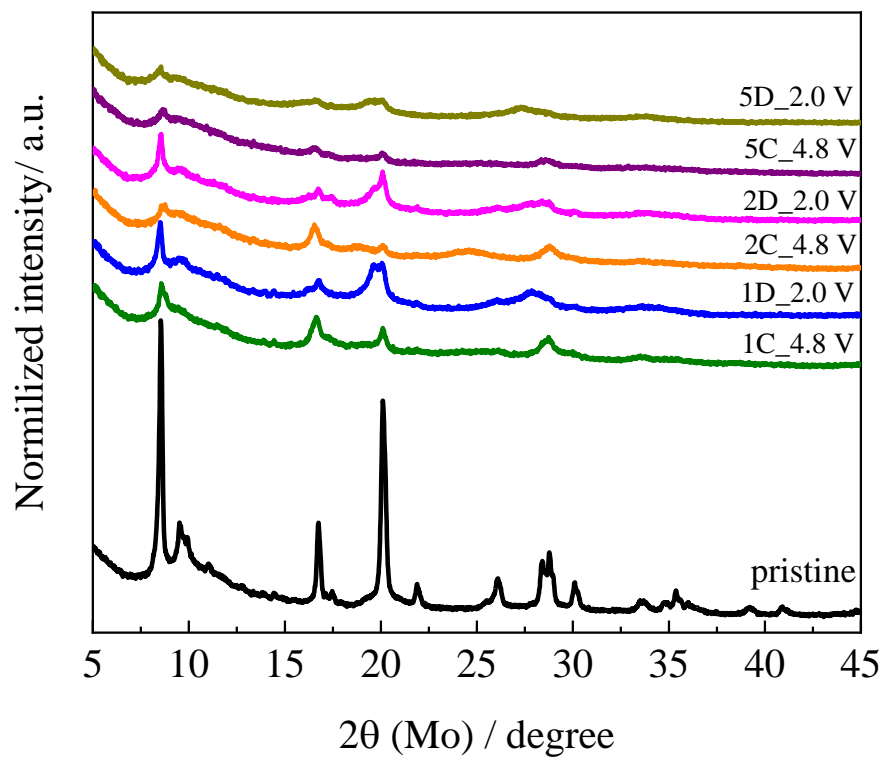
Figure 2. XRPD profiles for Li_2MnO_3 samples at pristine, and after the charged and discharged states in 1st, 2nd, and 5th cycles.

(a)

(b)

(c)

Li$_2$MnO$_3$ simulation

Li$_2$MnO$_3$ simulation
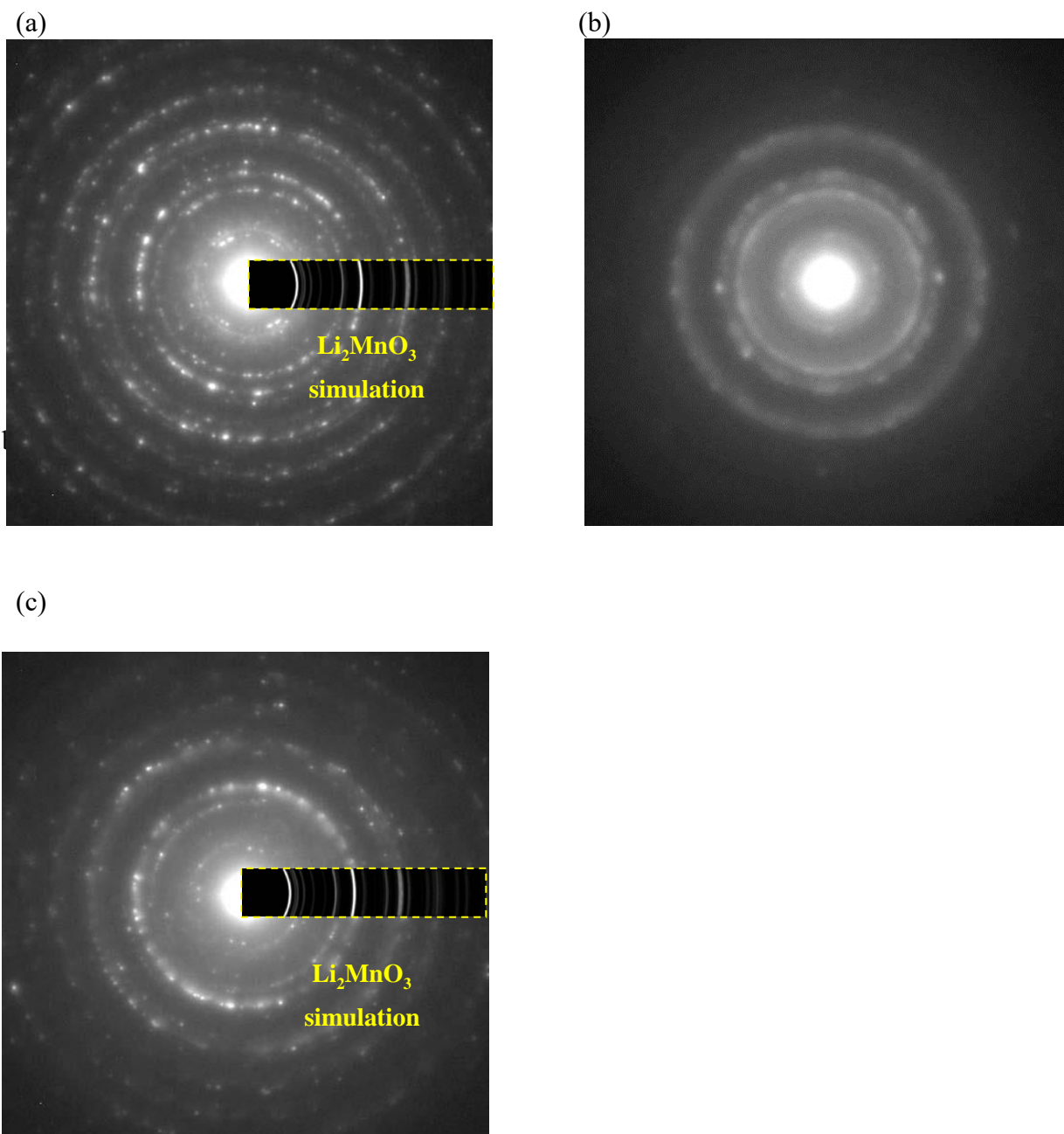
Figure 3. SAED obtained from TEM measurement for (a) pristine state, (b) 1st charged state, and (c) 1st discharged state.
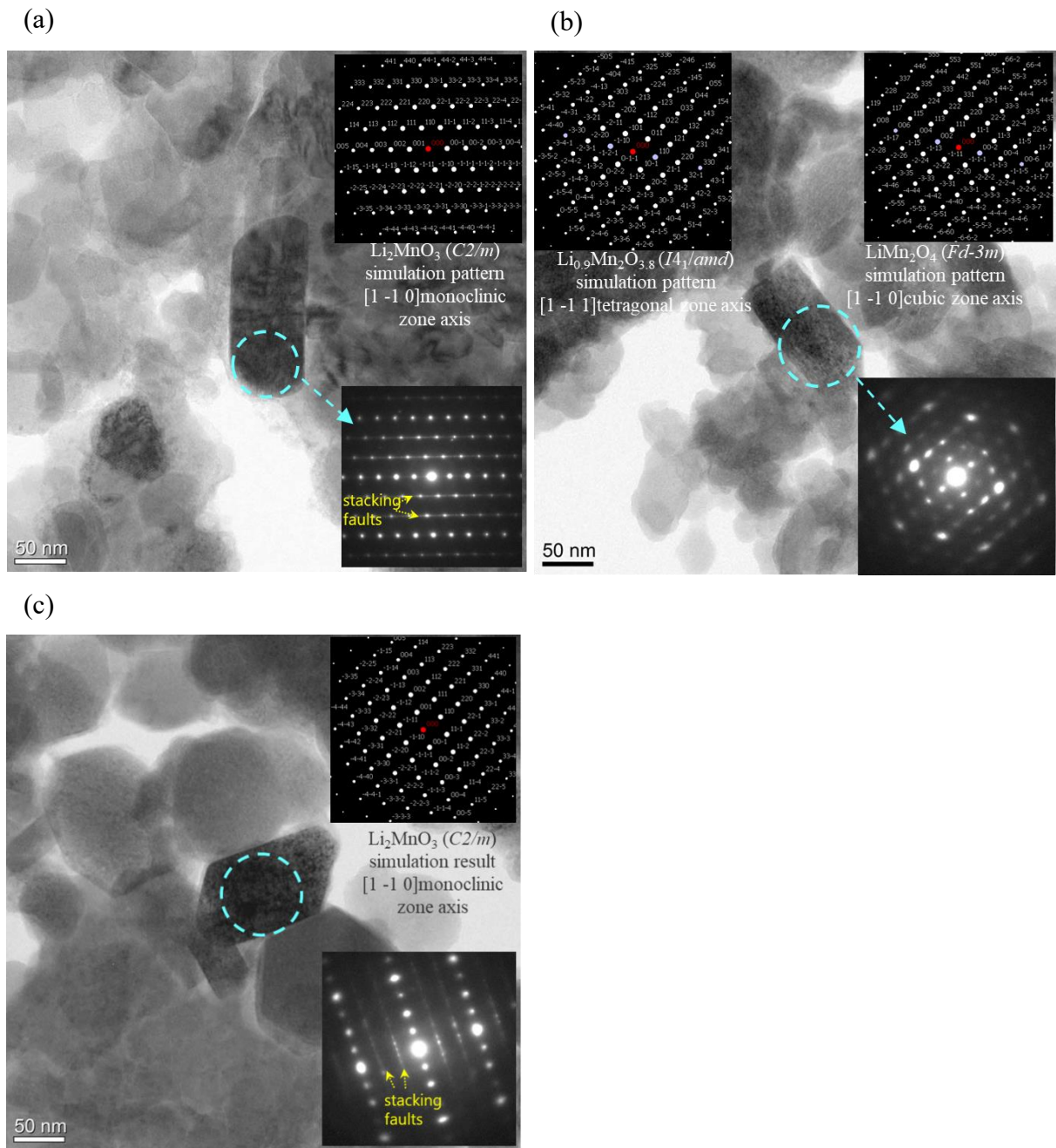
Figure 4. BF-STEM images and SAED patterns acquired along the [1-1-0] monoclinic zone axis of (a) pristine, (b) 1st charged, and (c) 1st discharged states of Li_2MnO_3.

(a)

(b)
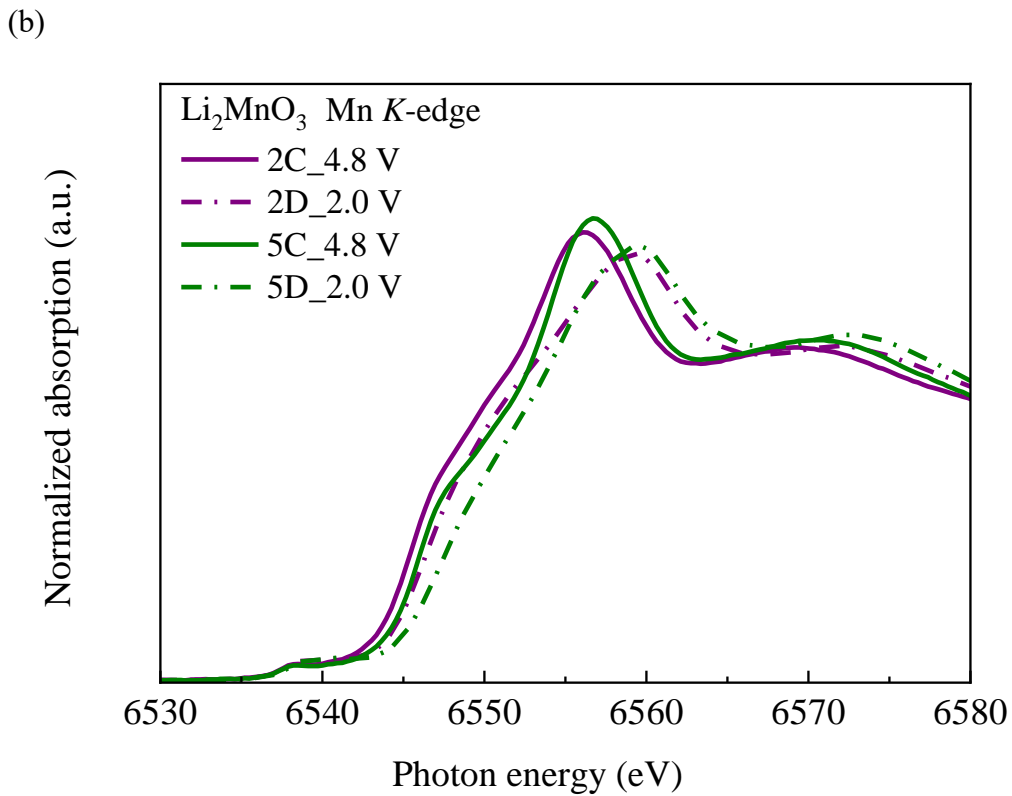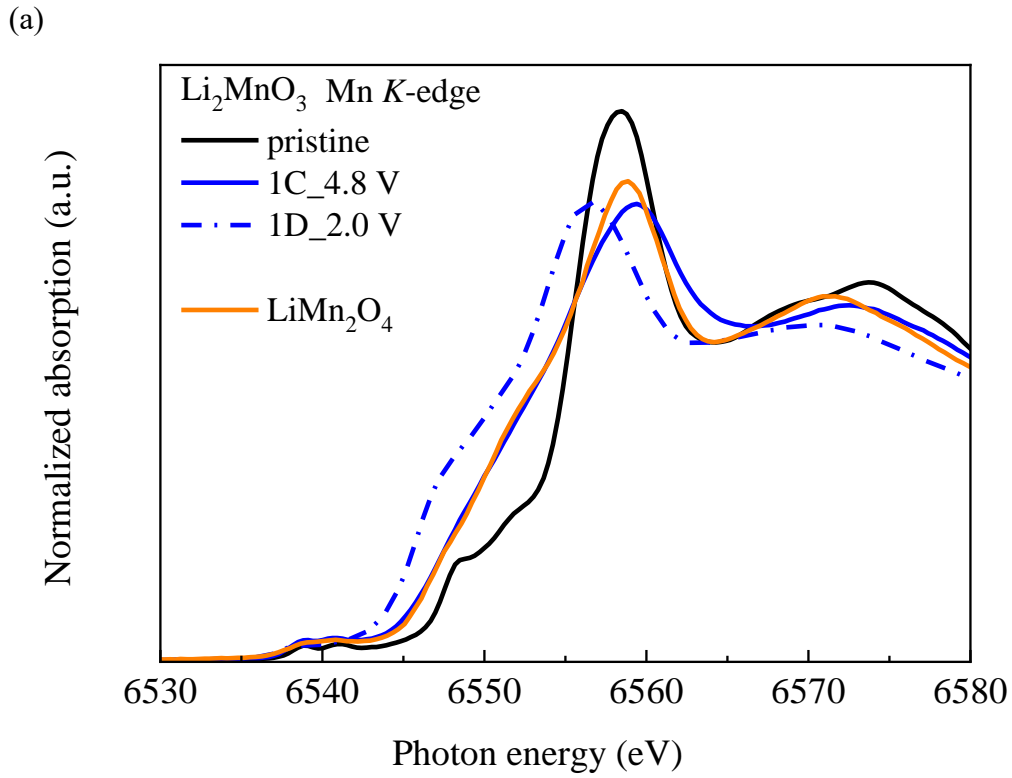
Figure 5. Mn K-edge XAFS spectra of Li_2MnO_3 at (a) the pristine, charged and discharged states of the 1st cycle, and (b) the 1st discharge and reversible 2nd and 5th cycles.
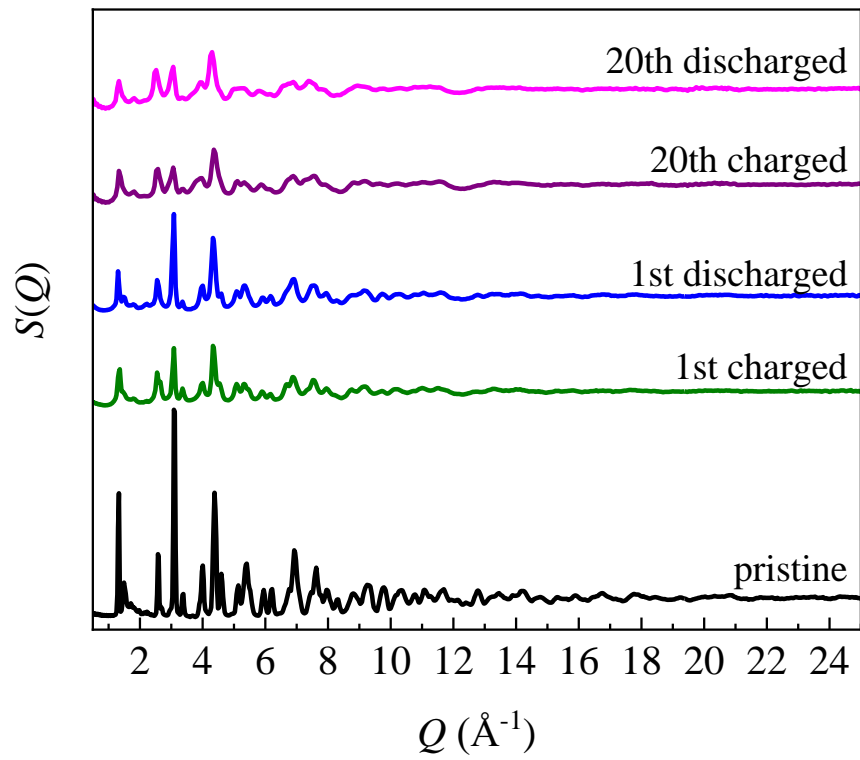
Figure 6. $S(Q)$ profiles of Li_2MnO_3 samples obtained by the X-ray total scattering experiments at 61.4 keV.

(a)

(b)
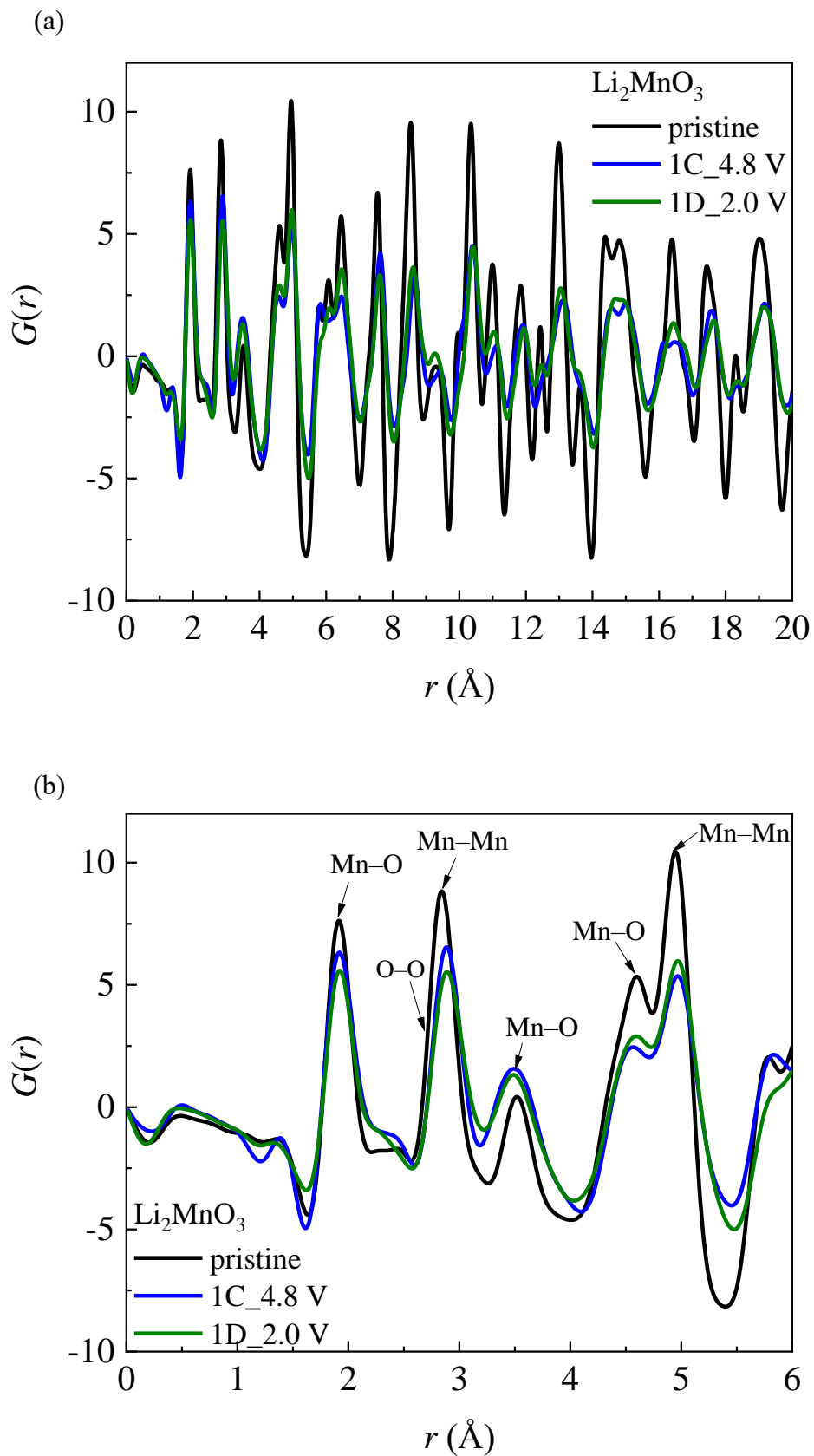
Figure 7. $G(r)$ profiles for the Li_2MnO_3 powder at (a) the pristine state, charged and discharged states of the 1st cycle, and (b) enlarged profiles in short-range region.
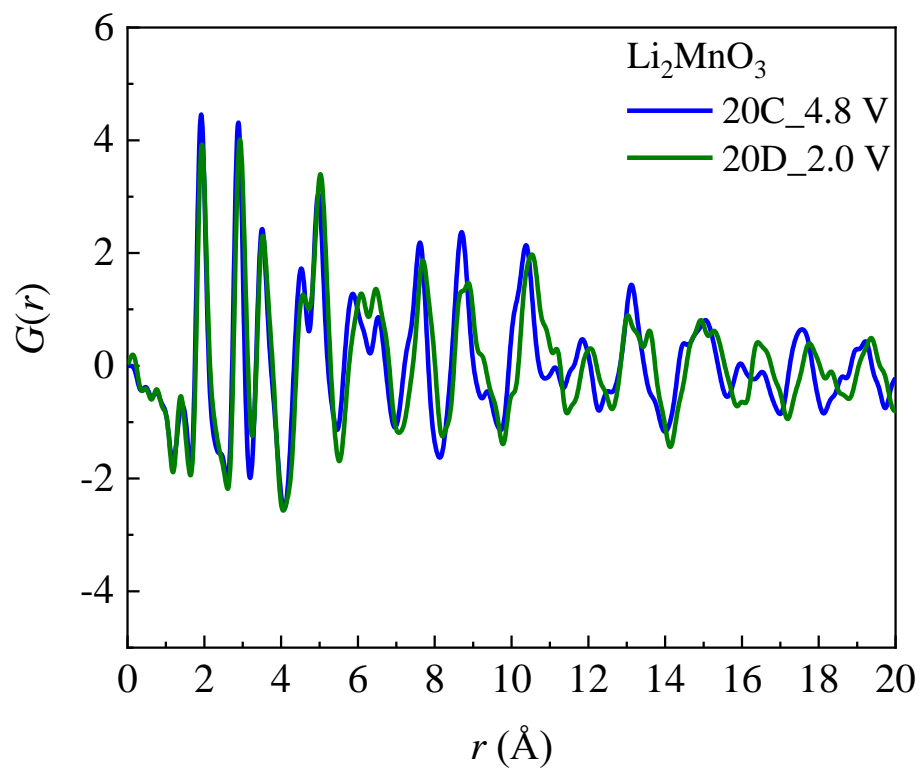
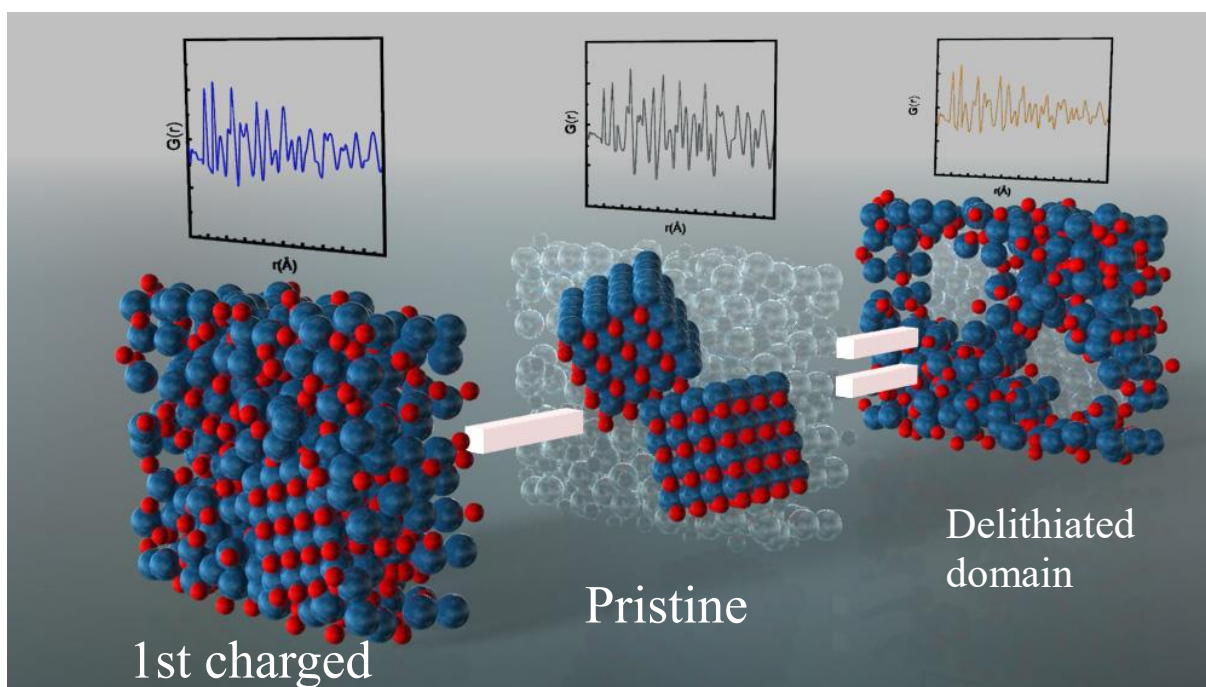Figure 8. *G*(*r*) profiles at the charged and discharged states in the 20th cycle.

Figure 9. Schematic diagram of differential PDF analysis. The $G(r)$ spectra of delithiated domain is obtained by extracting $G(r)$ of pristine from that of 1st charged state.
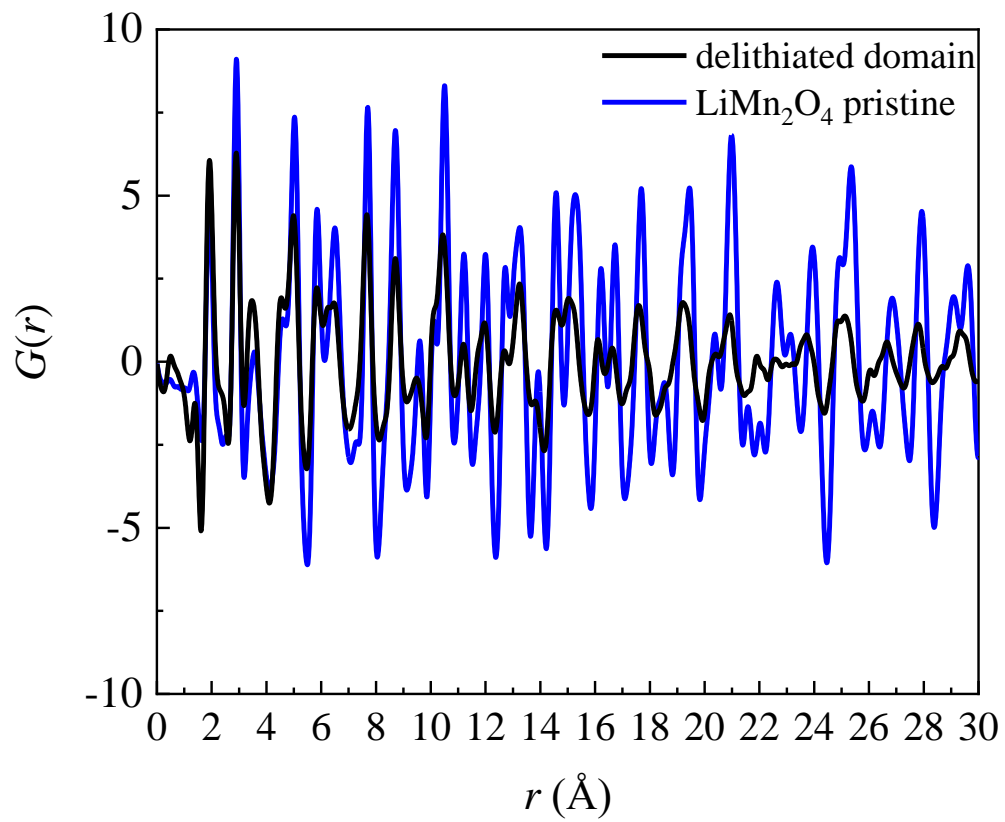
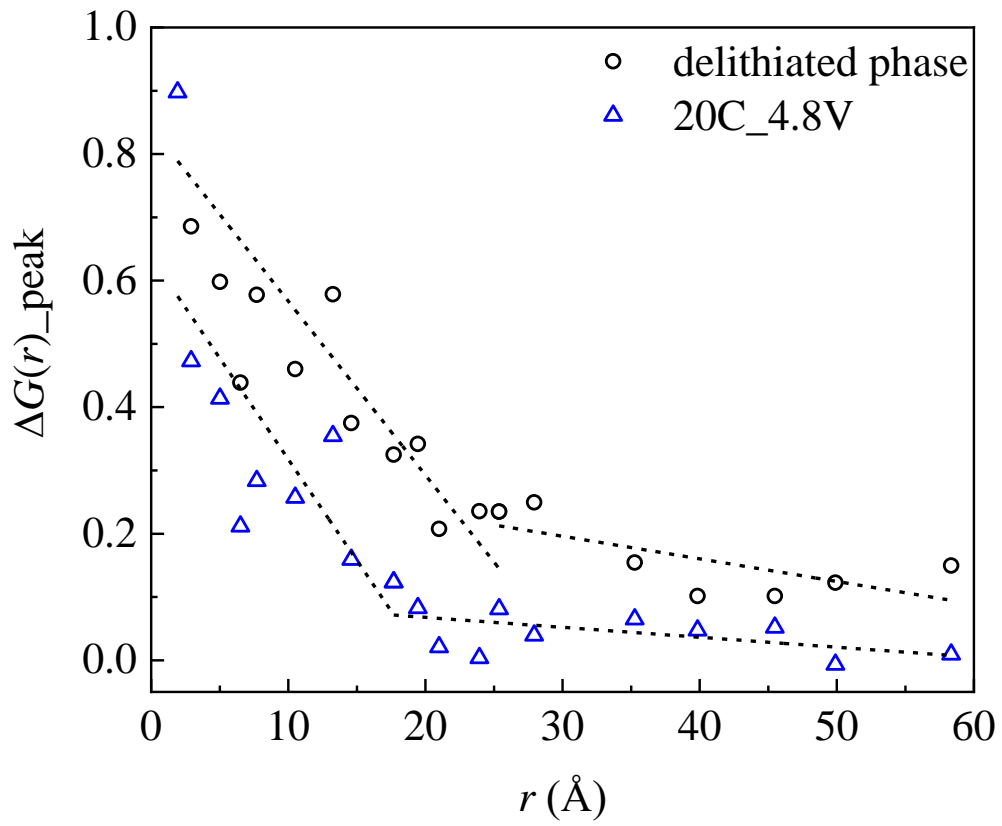Figure 10. $G(r)$ profiles of delithiated domain and the $LiMn_2O_4$ cubic spinel structure.

Figure 11. The $\Delta G(r)$_peak for the delithiated phase and 20th charge state, respectively, shown as a function of correlation distance, r.